

Temporal localized states and square-waves in semiconductor micro-resonators with strong time-delayed feedback

Elias R. Koch,¹ Thomas G. Seidel,¹ Julien Javaloyes,² and Svetlana V. Gurevich^{1,3,2, a)}

¹⁾*Institute for Theoretical Physics, University of Münster, Wilhelm-Klemm-Str. 9, 48149 Münster, Germany*

²⁾*Departament de Física & IAC-3, Universitat de les Illes Balears, C/ Valldemossa km 7.5, 07122 Mallorca, Spain*

³⁾*Center for Nonlinear Science (CeNoS), University of Münster, Corrensstrasse 2, 48149 Münster, Germany*

In this paper we study the dynamics of a vertically-emitting micro-cavity operated in the Gires-Tournois regime that contains a semiconductor quantum-well and that is subjected to strong time-delayed optical feedback and detuned optical injection. Using a first principle time-delay model for the optical response, we disclose sets of multistable dark and bright temporal localized states coexisting on their respective bistable homogeneous backgrounds. In the case of anti-resonant optical feedback, we identify square-waves with a period of twice the round-trip in the external cavity. Finally, we perform a multiple time-scale analysis in the good cavity limit. The resulting normal form is in good agreement with the original time-delayed model.

We theoretically study the dynamics of temporal localized states and square-waves in an injected micro-resonator enclosed into a long external cavity. Departing from former studies where only an intensity dependent refractive index (i.e. a Kerr nonlinearity) was used, we consider a semiconductor quantum well as the nonlinear element. A first principle time-delayed model for the optical response is employed. By conducting extended direct numerical simulations and utilizing path-continuation techniques, we demonstrate the existence of a bistable set of bright and dark temporally localized states as well as square-waves. To clarify the influence of the second and third order chromatic dispersion and of the relative position with respect to the band-gap frequency of the quantum well, we derive a normal form partial differential equation in the good cavity limit and compare its results with those obtained with the original time-delayed model.

structures (TLSs) and square-waves (SWs) was demonstrated^{11–13}. There, it was shown that the natural modeling approach consists in using singular time-delayed systems, in which the algebraic constraints simply corresponds to the boundary conditions linking the optical field in the various parts of the compound cavity system. In the normal dispersion regime and for the case of resonant optical feedback, dark and bright TLSs (and corresponding OFCs) appear via the locking of domain walls that connect the high and low bistable continuous wave (CW) intensity levels. Due to the oscillatory tails induced by the cavity dispersion¹⁴, these solutions can interlock at multiple equilibrium distances leading to a rich solution multistability. Moreover, operated out of the bistability regime and for anti-resonant feedback, SWs possessing a period of twice the round-trip in the external cavity were disclosed. Interestingly, the latter appear through a homoclinic snaking scenario leading to the formation of complex-shaped multistable solutions.

I. INTRODUCTION

Optical frequency combs (OFCs) denote light fields consisting of a discrete series of evenly spaced spectral components (or colors) that maintain high coherence across the whole bandwidth with ultra-low-noise¹. Their applications encompass a variety of fields including ultra-broadband coherent optical communications, high-precision optical spectroscopy, high precision metrology and optical arbitrary pulse generation^{2–5}, to name just a few. Prominent examples of OFCs realizations leverage the temporal cavity solitons obtained in injected passive high-Q Kerr resonators, such as microrings⁶ and fiber loops⁷ or employ active optical sources such as mode-locked lasers^{8–10}.

Recently, the promising potential of injected Kerr micro-cavities enclosed into a long external feedback cavity as sources of high-power tunable OFCs, temporal localized

Departing from former studies, in this paper we analyze the impact of considering a semiconductor quantum well as the nonlinear element. A first principle model for the optical response is employed which allows to explore e.g., the influence of the detuning with respect to the semiconductor band-gap that controls the ratio between nonlinear index change and absorption. Using a combination of analytical, numerical and path-continuation methods, we shall show that this extended model predicts the existence of a multistable set of bright and dark TLSs coexisting on their respective bistable homogeneous CW backgrounds. Furthermore, in the case of anti-resonant optical feedback, the dynamics of resulting SWs is analyzed. Finally, in order to clarify the influence of the second and third order chromatic dispersion and of the frequency dependence of the quantum-well response, we perform a multiple time-scale analysis in the good cavity limit. The resulting dispersive normal form partial differential equation shows a good qualitative agreement with the original time-delayed model.

^{a)}Electronic mail: gurevics@uni-muenster.de

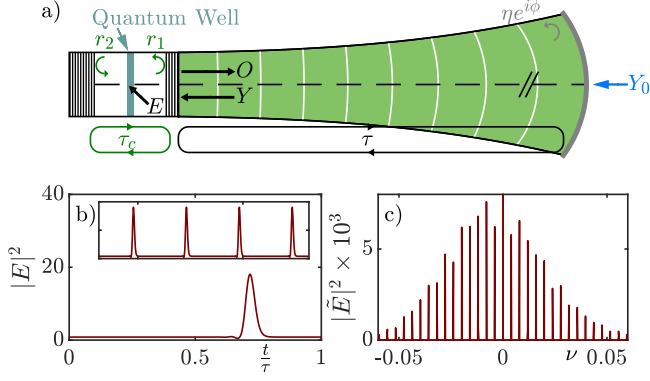


FIG. 1. a) Schematic of a micro-cavity containing a quantum well layer coupled to an external cavity with round trip τ which is closed by a mirror with reflectivity η and phase ϕ , and driven by a CW beam with amplitude Y_0 . b) A single TLS circulating in the external cavity obtained by a numerical integration of Eqs. (1)-(3). The inset shows the dynamics over several round-trips. c) Power density spectrum of the solution in b). Parameters are $(\delta, h, \eta, \phi, \gamma, f, u, b, \tau) = (0.015, 2, 0.99, 0, 1, 0.2, 0.65, 1000, 250)$.

II. MODEL EQUATIONS

The schematic setup is depicted in Fig. 1 (a). It is composed of a monomode micro-cavity of a few micrometers in length, with a radius up to $100 \mu\text{m}$ and with round-trip time τ_c , which contains a thin quantum well layer acting as a nonlinear medium that is situated at the anti-node of the field. The micro-cavity is closed by two distributed Bragg mirrors with reflectivities $r_{1,2}$ and it is coupled to a long external cavity of (typically) a few centimeters with round-trip time $\tau \gg \tau_c$. The system is subjected to CW injection with amplitude Y_0 and frequency ω_0 . The detuning with respect to the micro-cavity resonance ω_c is $\delta = \omega_c - \omega_0$. The external cavity is closed by a feedback mirror with reflectivity η . The total external cavity phase ϕ consists of the accumulated phase per round-trip due to propagation and the phase of the feedback mirror ϕ .

Following the methods developed in Refs. ^{11,15}, the first-principles model for the system shown in Fig. 1 (a) reads

$$\dot{E} = [if\chi - 1 - i\delta]E + hY, \quad (1)$$

$$\dot{D} = \gamma[-D + \Im(\chi)|E|^2], \quad (2)$$

$$Y = \eta e^{i\phi} [E(t - \tau) - Y(t - \tau)] + Y_0 \sqrt{1 - \eta^2}. \quad (3)$$

Here, E and Y denote the slowly varying envelope of electric fields in the micro-cavity and the external cavity, respectively. Further, D is the carrier density normalized to the transparency level at the band gap, γ is the scaled carrier lifetime, and f is an effective dimensionless gain prefactor. The latter is the product of a geometrical factor that contains the cavity enhancement effect and the active medium length, normalized by the photon lifetime in the micro-cavity. The field cavity enhancement can be conveniently scaled out using the Stokes relations allowing the fields E and Y to be of the same order of magnitude. This leads to a simple input-output relation $O = E - Y$: The output O is the combination of the intra-cavity

photons transmitted and reflected by the micro-cavity and it is re-injected after attenuation and a time delay τ . The coupling between the intra- and external cavity fields is given by Eq. (3) which is a delay algebraic equation (DAE). The DAE (3) takes into account all the multiple reflections in a possibly high finesse external cavity where $\eta \lesssim 1$.

The light coupling efficiency in the cavity is given by the factor $h = h(r_1, r_2) = (1 + |r_2|)(1 - |r_1|)/(1 - |r_1||r_2|)$ in Eq. (1). Here, we consider the case of a perfectly reflecting bottom mirror, i.e. $h = h(r_1, 1) = 2$ which corresponds to the so-called imbalanced Gires–Tournois interferometer regime¹⁶. These interferometers are widely used as optical pulse shaping elements¹⁷. They induce a controllable amount and sign of group delay dispersion (GDD), which is typically the dominating effect outside resonance. The amount and sign of GDD are tunable by choosing the frequency of operation with respect to the cavity resonance and around resonance where the second-order contribution vanishes and switches sign, third order dispersion (TOD) becomes the leading term¹⁴. Due to TOD, the resulting temporal pulses can possess oscillatory tails, see Fig. 1 (b), where a typical periodic time trace obtained from integrating numerically Eqs. (1)-(3) is shown. As a result, the envelope of the corresponding OFC is asymmetrical, see Fig. 1 (c).

Finally, $\chi = \chi(u, D)$ is a nonlinear susceptibility function. As a simple model, we employ the quantum well susceptibility as introduced in Ref. ¹⁸ as

$$\chi = \frac{1}{\pi} [\ln(u + i - b) - 2\ln(u + i - D) + \ln(u + i) - \ln(b)]. \quad (4)$$

The susceptibility χ describes the response of the medium to incoming light with frequency ω_0 . This analytical formula originates from assuming two parabolic bands with a quasi-equilibrium Fermi distribution for electron and holes. This response possesses both a real and an imaginary part that represents the non-instantaneous Kerr effect mediated by the population inversion, as well as the field saturable absorption, which also depends on D . Further, χ depends on u , the normalized frequency with respect to the band-gap frequency ω_G as $u = (\omega_0 - \omega_G)/\gamma_{\perp}$, where γ_{\perp} is the intraband polarization dephasing rate. The parameter b relates to the top-band frequency ω_T , and reads $b = (\omega_T - \omega_G)/\gamma_{\perp}$. The gain (or the saturable absorption) is defined as $-\Im(\chi)$ while the phase shift caused by the nonlinear refraction index is described by $\Re(\chi)$.

The situation where $D = 0$ describes an empty conduction band and a transition from transparency to saturable absorption located around $u = 0$ while $D = 1$ corresponds to the optical transparency being reached at the bandgap, i.e. $\Im[\chi(0, 1)] = 0$. The real and negative imaginary parts of the susceptibility χ are represented for different values of the population inversion in Fig. 2.

III. BIFURCATION ANALYSIS OF THE DAE SYSTEM

To understand the origin and the behaviour of the periodic pulse solution presented in Fig. 1 (b), we perform a bifurca-

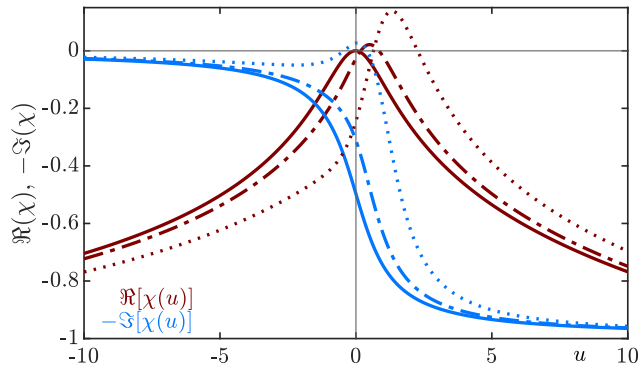


FIG. 2. The real (red) and negative imaginary (blue) parts of the susceptibility $\chi(u, D)$ as given by Eq. (4) for $b = 100$ for $D = 0.3$ (dash-dotted line) and $D = 1.08$ (dotted line) which enclose the range of D for the parameter set used in Fig. 1 as well as $D = 0$ (solid line).

tion analysis of the system (1)-(3) using a recently developed extension of DDE-BIFTOOL¹⁹ that allows for the bifurcation analysis of algebraic and neutral delayed equations^{12,13,20–22}. We start the analysis with the situation where the injection is set to be resonant with an external cavity mode, i.e., $\varphi = 0$. In the long-delay limit, where the time delay is the longest relevant time scale and in conjunction with sufficiently large detuning δ , the quantum well nonlinearity causes a bistable CW response of the system in a certain parameter range of the injection intensity. We show in Fig. 3 (a) the resulting hysteresis diagram depicted in blue for the same parameter set used in Figs. 1 (b,c). The stability is indicated by the line thickness. One can see that the CW branch loses stability in a saddle-node (SN) bifurcation at the point SN_1 and regains it in another SN bifurcation at SN_2 . From the CW branch, one observes that the branch of the TLSs emerges in a subcritical Adronov–Hopf bifurcation. Indeed, in the bistable CW region, similar to the case of the injected microcavity subjected to the Kerr nonlinearity^{11,12}, the coexistence of two stable CW solutions can lead to the formation of domain walls between them that exhibit oscillatory tails, for certain sets of parameters. In particular, two opposed fronts may lock at discrete distances forming stable bound states which results in the formation of TLSs. The corresponding branch of periodic solutions (cf. red line in Fig. 3 (a)) features stable dark and bright TLSs over an extended injection range. Here, different stable and unstable locking ranges occur along a collapsed snaking structure^{23,24} around a Maxwell line where opposing fronts have the same drifting speed, see the insets in panel (a). On the left or the right of the Maxwell line, the drifting speeds differ, leading to a transient towards the lower or the upper CW state, respectively. Figure 3 (b,c) show two exemplary dark and bright solution profiles at different positions along the snaking branch. Remarkably, one notices that although being calculated for very close values of Y_0 , the dark TLS shows a stronger oscillatory tail, while the snaking is more pronounced in the vicinity of the lower CW state, i.e., for the bright solutions. A video showing the whole evolution of the

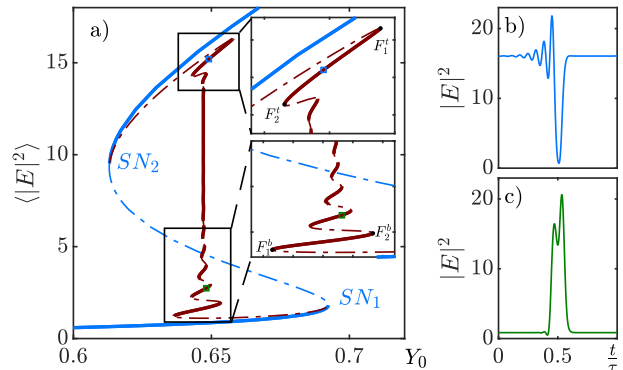


FIG. 3. (a) Branches of CW (blue) and TLSs (red) solutions of Eqs. (1)-(3) as a function of the injection Y_0 . Thick (thin) lines denote stable (unstable) solutions, respectively. The insets show zooms around the upper and lower snaking regions. In the right panels two exemplary dark (b) and bright (c) solution profiles at positions labeled with a blue and green square in (a) are displayed. Parameters as in Fig. 1 (b,c).

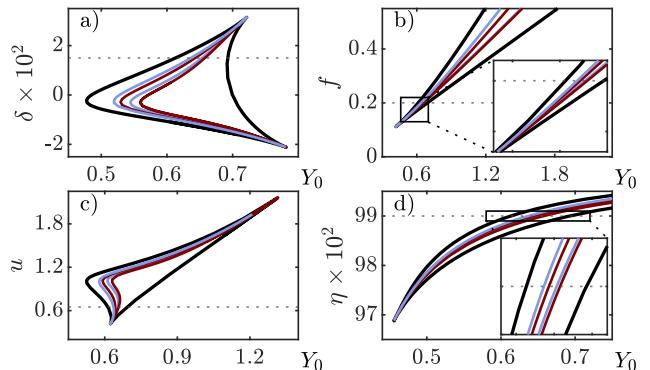


FIG. 4. (a)-(d) Two-parameter bifurcation diagrams in (Y_0, δ) , (Y_0, f) , (Y_0, u) and (Y_0, η) planes, respectively. Evolution of the points SN_1 and SN_2 limiting the region of CW bistability (black) is shown together with the two major folds limiting the stability of the dark (dark red) and bright (light blue) TLSs, respectively. The horizontal dashed lines indicate the particular parameter values used in Fig. 3. Other parameters as in Figs. 1, 3.

TLS solution along the branch is presented in Supplementary Material.

To investigate the existence and the stability borders of the obtained TLSs solutions in this parameter regime, four two-parameter continuations in (Y_0, δ) , (Y_0, f) , (Y_0, u) and (Y_0, η) planes are carried out and the results are presented in Fig. 4 (a)-(d), respectively. Here, black lines correspond to the thresholds of the SN bifurcation points SN_1 and SN_2 limiting the region of CW bistability, whereas dark red and light blue lines show the evolution of the two major folds limiting the stability of the dark and bright TLSs, respectively, cf. $F_{1,2}^{t,b}$ in the insets of Fig. 3 (a). The horizontal dashed line indicate the particular parameter values used in Fig. 3.

In particular, in Fig. 4 (a) one can see that the CW bistable region exists for both anomalous and normal dispersion

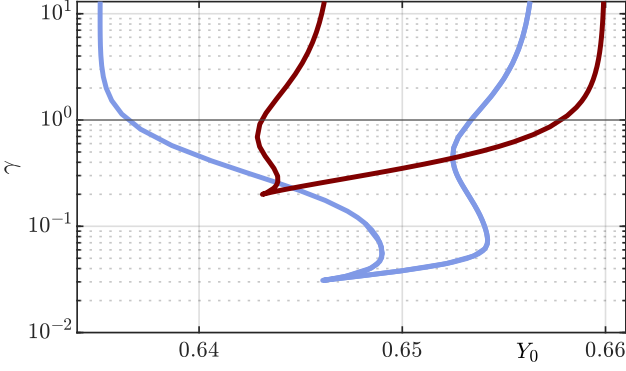


FIG. 5. Two-parameter bifurcation diagram in the (Y_0, γ) plane showing the evolution of the major folds of the dark (dark red) and bright (light blue) TLSs. The horizontal black line indicates the particular parameter value used in Fig. 3. Other parameters as in Figs. 1, 3.

regimes and the stability regions of both bright and dark TLSs is broader for small detunings and injection values. The latter vanish for large values of δ and Y_0 . A similar trend is presented in panel (c), where the diagram in the (Y_0, u) plane is shown. Here, one observes that the bistability region opens only in a certain range around $u \sim 1$, which corresponds to the most efficient nonlinear modulation of the losses. Again, the region of stable existence for TLSs decreases for increasing injection values. Figure 4 (b) presents the evolution of the corresponding folds in the effective gain prefactor f . Here, the bistability region starts to exist for small finite values of f and small detuning values and it is becoming broader with increasing f , hence for stronger nonlinearity; the fold lines of both dark and bright TLSs follow the same trend. In panel (d), the dynamics of the limiting folds is shown in the (Y_0, η) plane. Hence, the TLSs solutions exist and are stable only in the so-called good cavity limit, where $\eta \rightarrow 1$. Moreover, the corresponding regions are moving in the direction of larger injections with increasing η . Note that this analysis was carried out for $\gamma = 1$, i.e. assuming that the carrier lifetime is equal to the photon lifetime in the cavity, a situation that typically corresponds to a fast saturable absorber with a relaxation rate in the picosecond range.

Finally, we present in Fig. 5 a continuation in the carrier lifetime γ . Here, the evolution of the major folds limiting the stability of the dark (dark red) and bright (light blue) TLSs is shown, cf. the inset in Fig. 3 (a). One can see that for increasing γ values, first bright TLSs start to exist and the bistability between dark and bright TLSs is established only above some finite value of γ . Moreover, the width of the stability regions remains constant for large γ values, where the adiabatic elimination of the carriers can be performed, connecting our results with past studies based upon an instantaneous nonlinearity^{11–13}.

IV. DISPERSIVE MASTER EQUATION

Although the bifurcation analysis allows for quantitative predictions of the behavior of the DAE system (1)-(3), an intuitive interpretation of the dynamics presented in Fig. 3 is difficult since the role and impact of e.g., GDD and TOD on the TLS formation is hidden. Hence, to obtain a better understanding of the underlying physical mechanisms, we derive a partial differential equation (PDE) that approximates the dynamics of the full DAE model (1)-(3) in the limit of a good cavity ($\eta \rightarrow 1$) and small detunings δ using a rigorous multiple time scale analysis as discussed in^{12,14,21,25}. We start our analysis by eliminating the field $Y(t)$ and transforming the DAE to a neutral delay differential equation (NDDE) that reads

$$\eta \dot{E}(t - \tau) + \dot{E}(t) = \eta [if\chi(D(t - \tau)) - 1 - i\delta + h]E(t - \tau) + [if\chi(D(t)) - 1 - i\delta]E(t) + hY_0\sqrt{1 - \eta^2}. \quad (5)$$

Further, rescaling time with respect to the time-delay τ reveals a natural smallness parameter $\varepsilon = \tau^{-1}$, where $\varepsilon \ll 1$ in the long-delay limit. In the next step rescalings are chosen as $E \rightarrow \varepsilon^{\frac{1}{2}}\mathcal{E}$, $Y \rightarrow \varepsilon^{\frac{1}{2}}\mathcal{Y}$, $Y_0 \rightarrow \varepsilon^{\frac{1}{2}}\mathcal{Y}_0$, and $D \rightarrow \varepsilon\mathcal{D}$. This choice of the scaling is also reflected in the treatment of the nonlinearity which now becomes $\chi(\varepsilon\mathcal{D})$. Hence, the obvious next step is an expansion of χ , leading to

$$\chi(\varepsilon\mathcal{D}) = \chi(0) + \varepsilon\chi'(0)\mathcal{D} + \mathcal{O}(\varepsilon^2), \quad (6)$$

where we omitted the u dependence for brevity and

$$\begin{aligned} \chi(0) &= \chi_0 = -\frac{1}{\pi} \ln(-u - i) \\ &= \frac{-1}{\pi} \ln \sqrt{u^2 + 1} + i \left[\frac{1}{2} + \frac{1}{\pi} \arctan(u) \right], \quad (7) \\ \chi'(0) &= \chi'_0 = \frac{2}{\pi} \frac{u - i}{u^2 + 1}. \end{aligned}$$

The dynamics is now considered on multiple timescales in powers of ε . To this aim, the remaining fields and parameters are all expanded in powers of ε . In addition, the fastest timescale $\sigma = \omega t$ is also stretched by expanding ω in powers of ε in order to account for the fact that the period T is slightly larger than the time delay τ . Hence, σ describes the fast dynamics within one period.

After inserting all expansions into the NDDE (5), one collects orders of ε and solves them separately imposing the proper solvability conditions, see Supplementary Material for details. Finally, we find that the dispersive master PDE for the field E on a fast timescale σ containing the dynamics within one round-trip and an effective slow timescale θ that describes the dynamics over many round-trips, reads

$$\partial_\theta E = (-id_2 \partial_\sigma^2 + d_3 \partial_\sigma^3)E + (\mathcal{L} + \mathcal{N}D)E + hY_0 \frac{\sqrt{1 - \eta^2}}{1 + i\delta}. \quad (8)$$

Here, the values of the coefficients d_2 and d_3 of the linear spatial operator in Eq. (8) are particularly instructive and read

$$d_2 = \frac{2\delta}{(1 + \delta^2)^2}, \quad d_3 = \frac{2}{3} \frac{3\delta^2 - 1}{(1 + \delta^2)^3}, \quad (9)$$

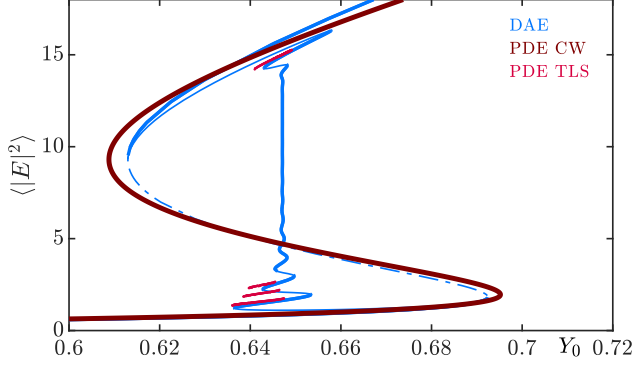


FIG. 6. CW and exemplary numerical TLS solutions of the PDE system (8)-(11) plotted together with the branches from Fig. 3 of the DAE (1)-(3). Also, some parameter values have been adjusted for the PDE results, since bistability is lost for the exact set of parameters that has been used in Figs. 1, 3. The adjusted parameters are $u = 0.52$, $\delta = 0.044$ and $\gamma = 10$. The corresponding PDE parameters are shown in Table I.

whereas the coefficients \mathcal{L} and \mathcal{N} are

$$\begin{aligned}\mathcal{L} &= \eta - 1 - 2\eta \arctan(\delta) i + 2f \left(\frac{1 - i\delta}{1 + \delta^2} \right)^2 \chi_0 i, \\ \mathcal{N} &= 2f \frac{1 - i\delta}{1 + \delta^2} \chi_0' i,\end{aligned}\quad (10)$$

Further, the equation for the carrier density D takes the form

$$\gamma^{-1} \partial_\sigma D = -D + \Im(\chi_0 + \chi_0' D) |E|^2. \quad (11)$$

One can see that the second order dispersion coefficient d_2 in Eq. (8) cancels at resonance, i.e., at $\delta = 0$, corresponding to the transition from anomalous to normal dispersion regime. Hence, at small δ values the dynamics is mostly controlled by TOD, which explains the oscillating tails of the TLSs observed in Fig. 3. Further, TOD vanishes for $\delta = \delta_c = \pm 1/\sqrt{3}$.

Note that the linear operator in Eq. (8) corresponding to the case of the linear empty cavity (i.e., $D = 0$ (and $\chi = 0$)) coincides with the linear part of the normal form PDE derived for the case of a quasi-conservative dispersive microcavity containing a Kerr medium coupled to a distant external mirror²¹. There, a similar multiscale analysis performed in the long delay limit for small cavity losses and weak injection yielded the Lugiato-Lefever equation with TOD²⁶⁻²⁸. The latter can be understood as a dissipative version of the nonlinear Schrödinger equation in which the phase symmetry is broken by the presence of monochromatic injection with amplitude Y_0 and frequency offset δ with respect to the microcavity resonance. In the presence of the nonlinear element, the corresponding contributions depending on χ_0 , χ_0' , f as well as δ appear in the coefficients \mathcal{L} , \mathcal{N} , cf. Eqs. (10).

The CW solution ($E_s, D(E_s)$) of Eqs. (8)-(11) can be found

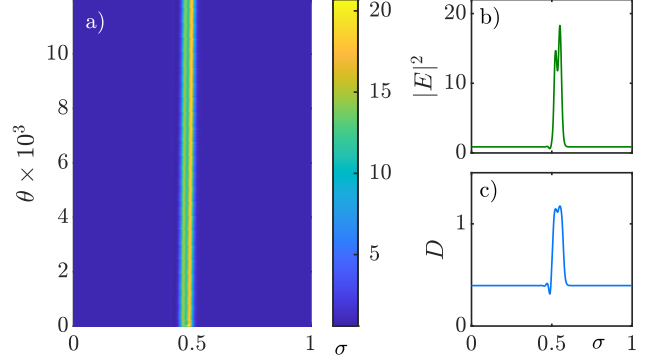


FIG. 7. (a): Space-time evolution of a bright TLS obtained from the numerical simulations of the PDE model (8)-(11) for $Y_0 = 0.6437$ (b),(c): Exemplary profiles taken at the last time-step showing the intensity $|E|^2$ and D , respectively.

analytically by solving them for Y_0 yielding

$$Y_0^2 = \frac{1 + \delta^2}{h^2(1 - \eta^2)} |\mathcal{L} + \mathcal{N} D(I_s)|^2 I_s, \quad (12)$$

$$D(I_s) = \frac{\Im(\chi_0) I_s}{1 - \Im(\chi_0') I_s}, \quad (13)$$

where $I_s = |E_s|^2$.

Notice that the CW states (12)-(13) does not exhibit a bistability region for the same parameter set as the CW solution obtained from the DAE system parameters corresponding to the solution presented in Fig. 3. However, for a slightly different set of system parameters where the parameters that were scaled or expanded during the PDE (8)-(11) derivation are adjusted, the bistability region is established and almost identical to the results obtained from the DAE system (1)-(3), see Fig. 6. Here, the DAE CW and TLS solutions (blue) are plotted together with the corresponding PDE CW (dark red) and exemplary TLS (light red) solutions, obtained by means of direct numerical simulations. The corresponding PDE coefficients are presented in Table I.

The observed discrepancy can be ascribed to the fact that assumption of a small population inversion $D \ll 1$ is not always strictly verified, see for instance Fig. 7 (c) and Fig. 8 (c) where D is of order $\mathcal{O}(1)$ during TLS emission, but also on the CW background.

d_2	0.088
d_3	-0.659
\mathcal{L}	-0.271 - 0.079i
\mathcal{N}	0.204 + 0.095i
χ_0	-0.038 + 0.653i
χ_0'	0.261 - 0.501i

TABLE I. Coefficients for the PDE (8)-(11) solutions presented in Fig. 6. Other parameters are as in Fig. 3

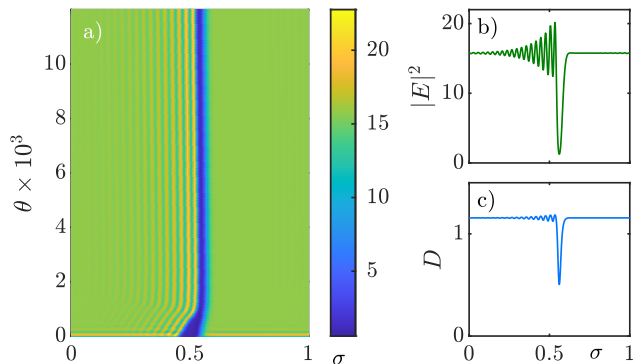


FIG. 8. (a): Space-time evolution of a dark TLS obtained from the numerical simulations of the PDE model (8)-(11) for $Y_0 = 0.6491$. (b),(c): Exemplary profiles taken at the last time-step showing the intensity $|E|^2$ and D , respectively.

In order to compare the solutions of the normal form (8)-(11) with those obtained from the full DAE model (1)-(3), we solved the PDE master equations (8)-(11) numerically for the adjusted parameter set from Fig. 1 and Fig. 3. The direct numerical simulations were performed using a standard split-step based pseudo-spectral method²⁹. The carrier equation (11) was integrated using a dynamical boundary condition as in³⁰.

To visualize the evolution of the resulting solution over many round-trips, a space-time representation in (σ, θ) plane is employed and the results are presented in Figs. 7, 8. Figure 7 (a) shows the time evolution of a bright TLS. The corresponding profiles at the end of the simulations are presented in panels (b) and (c) for the intensity $|E|^2$ and carrier density D , respectively. Here, one can see that the domain walls lock at the second locking distance and the corresponding profile agrees with the bright TLS found in the DAE system, cf. Fig 3 (c). An example of a dark TLS is shown in Fig. 8 (a). The initial condition evolves into a dark TLS with strong asymmetric oscillatory tail as seen in an exemplary profiles in (b) and (c) for E and D , respectively. Again, this solution is in good agreement with the dark TLS found in the original DAE model, see Fig 3 (b). Note that both dark TLSs from the PDE and DAE possess more oscillatory tails as the bright TLSs. This situation is similar to the one observed for the Lugiato-Lefever equation subjected to TOD in the normal dispersion regime²⁸. There, TOD allows for stable dark and bright TLSs to coexist, while the shape of the switching waves connecting the top and bottom CW solutions is modified and bright TLSs are stabilized due to the generation of additional oscillations in the switching-wave profiles.

V. SQUARE-WAVES

Finally, we consider the same system given by DAE (1)-(3) but operated out of the bistability regime such that the wavelength of the optical injection is set in-between two modes of the external cavity. This situation corresponds to the case of

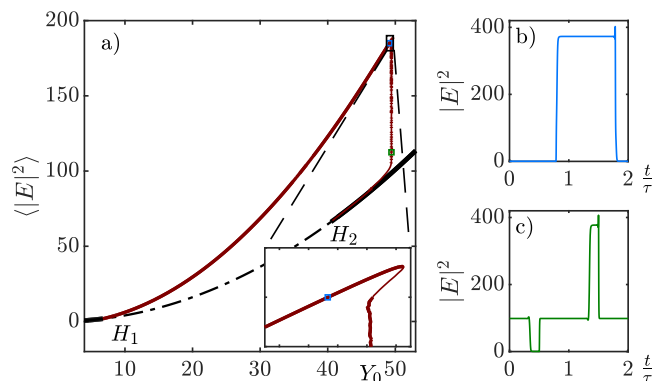


FIG. 9. SWs emerging in a supercritical AH bifurcation at H_1 and a subcritical AH bifurcation at H_2 . Such a branch will be referred to as a subcritical SW branch of the QGTI. b) shows a stable SW with 50% duty cycle, while c) shows a solution with three plateaus at the Maxwell line. $(\delta, h, \eta, \phi, \gamma, f, u, b, \tau) = (-0.01, 2, 0.98, \pi, 0.1, 1, 0.65, 1000, 1000)$.

antiresonant feedback, i.e. $\phi = \pi$.

Note that the formation of SWs was reported in various optical and opto-electronic systems subjected to time-delayed feedback³¹⁻³⁵. There, they typically appear in the long delay limit via a supercritical Andronov-Hopf (AH) bifurcation as modulated oscillations with a period close to twice the value of the time-delay τ . The SWs then evolve into sharp transition layers connecting plateaus of duration $\sim \tau$. Recently, the formation of SWs in a monomode micro-cavity containing a Kerr medium coupled to a long external feedback cavity under CW injection in the normal dispersion regime was demonstrated¹³. There, SWs also appear via a homoclinic snaking scenario, leading to the formation of complex-shaped multi-stable SW solutions. To study the formation and the properties of the SWs in the DAE model (1)-(3), we perform the path-continuation as a function of the injection Y_0 , setting the feedback phase $\phi = \pi$. Our results are shown in Fig. 9. In Fig. 9 (a), for increasing Y_0 , a branch of stable SW solutions (dark red) emerges from the stable CW state (black) at a supercritical AH bifurcation at the point H_1 . Here, a small-amplitude periodic solution with a period $\sim 2\tau$ close to the bifurcation point transforms into a well-developed SW with sharp transition layers when Y_0 is increased, see Fig. 9 (b), where the exemplary profile is shown (cf. the blue point in the panel (a)). However, for further increased Y_0 , the SW branch turns in a saddle-node bifurcation (cf. the inset in the panel (a)) and experiences a sequence of further saddle-node bifurcations resulting in a collapsed snaking structure. In particular, close to the vertical Maxwell line where the plateaus shrink in favor of the CW value, it leads to a three-plateau solution as shown in panel (c). Finally, the SW branch merges with the CW state at H_2 in a subcritical AH bifurcation. A video showing the whole evolution of the SW solution along the branch is presented in Supplementary Material. Remarkably, the snaking scenario is similar to one reported in¹³, where, however, it was observed for low injection values, whereas in the present case the subcritical AH bifurcation is

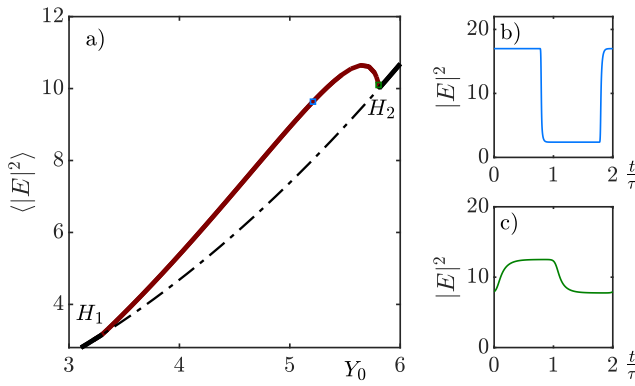


FIG. 10. An exemplary branch for the supercritical regime, close to the transition from sub- to supercritical SW solutions. The two profiles in b) and c) show a fully developed as well as a just emerging SW, respectively. The parameters are $(\delta, h, \eta, \varphi, \gamma, f, u, b, \tau) = (-0.01, 2, 0.86, \pi, 0.1, 1, 0.65, 1000, 1000)$.

created at high Y_0 .

By varying η to lower values one can observe a transition of the AH bifurcation at H_2 from subcritical to supercritical, which leads to a disappearance of the snaking structure. The transition seems to be located close to the SWs existing threshold in η . A resulting branch can be seen in Fig. 10 (a). While panel (b) demonstrates an exemplary profile of a fully developed SW with sharp transition layers, panel (c) shows a smoother periodic solution close to the (now) supercritical AH bifurcation at H_2 .

CONCLUSION

In conclusion, in this paper the dynamics of temporal localized states and square-waves in semiconductor micro-resonators with strong time-delayed feedback was analyzed. We considered a semiconductor quantum-well as the nonlinear element instead of an ideal, instantaneous Kerr response. This allowed us to study the influence of the band-gap detuning with respect to the injection field and the population inversion time scale onto the dynamics. A first principle model for the optical response was used in combination with time delayed algebraic constraints that correspond to the boundary conditions linking the optical field in the various parts of the compound cavity system.

Using a combination of analytical, numerical and path-continuation methods, the existence of dark and bright temporal localized states appearing via the locking of domain walls that connect the high and low bistable continuous wave intensity levels was demonstrated in the normal dispersion regime and for resonant feedback. Further, operated in the antiresonant (pi-shifted) feedback regime, square-waves solutions possessing a period of approximately twice the round-trip in the external cavity were obtained. Depending on the reflectivity of the external mirror, the latter can also appear through a homoclinic snaking scenario. Finally, to clarify the role of the second and third order dispersion in the formation of the local-

ized states, a multiple time-scale analysis in the good cavity limit was performed. The resulting dispersive normal form partial differential equation shows a good qualitative agreement with the original time-delayed model.

More generally, the results presented here may serve as a guide for further analysis into the dynamics of temporal localized states in semiconductor micro-resonators subjected to the strong time-delayed feedback in the long cavity regime. Our analysis clarified that, even in the good cavity limit, when the carrier lifetime becomes much smaller than the micro-cavity photon lifetime, both branches of bright and dark TLSs disappear, even if CW optical bistability is not affected. This indicates that the most favorable situation would certainly consider a quantum-well medium optimized to act as a saturable absorber with a fast carrier recovery time in the picosecond range instead of, e.g., a micro-cavity containing a gain medium engineered to favor a lasing action and for which the carrier lifetime would be in the nanosecond range.

SUPPLEMENTARY MATERIAL

See supplementary material for the animation showing the solution profiles along the branches shown in Figs. 3 and 9 in Sec. III and Sec. V, respectively and for details on the derivation of the normal form partial differential equation presented in Sec. IV.

AUTHOR DECLARATIONS

The authors have no conflicts to disclose.

ACKNOWLEDGMENTS

T.S. thanks the foundation ‘‘Studienstiftung des deutschen Volkes’’ for financial support, E.K, J. J. and S.G. acknowledge the financial support of the projects KEFIR, Ministerio de Economía y Competitividad (PID2021-128910NB-I00 AEI/FEDER UE) and KOGIT, Agence Nationale de la Recherche (ANR-22-CE92-0009), Deutsche Forschungsgemeinschaft (DFG) via Grant Nr. 505936983. We thank A. Giacomotti and B. Garbin for useful discussions.

DATA AVAILABILITY

The data that support the findings of this study are available from the corresponding author upon reasonable request.

REFERENCES

- ¹S. T. Cundiff and J. Ye, *Rev. Mod. Phys.* **75**, 325 (2003).
- ²T. Udem, R. Holzwarth, and T. W. Hänsch, *Nature* **416**, 233 (2002).
- ³S. T. Cundiff and A. M. Weiner, *Nature Photonics* **4**, 760 (2010).
- ⁴S. A. Diddams, *J. Opt. Soc. Am. B* **27**, B51 (2010).

- ⁵A. Pasquazi, M. Peccianti, L. Razzari, D. J. Moss, S. Coen, M. Erkintalo, Y. K. Chembo, T. Hansson, S. Wabnitz, P. Del'Haye, X. Xue, A. M. Weiner, and R. Morandotti, *Physics Reports* **729**, 1 (2018).
- ⁶T. Herr, V. Brasch, J. D. Jost, C. Y. Wang, N. M. Kondratiev, M. L. Gorodetsky, and T. J. Kippenberg, *Nature Photonics* **8**, 145 (2014).
- ⁷F. Leo, S. Coen, P. Kockaert, S. Gorza, P. Emplit, and M. Haelterman, *Nat Photon* **4**, 471 (2010).
- ⁸A. C. Tropper, H. D. Foreman, A. Garnache, K. G. Wilcox, and S. H. Hoogland, *J. Phys. D: Appl. Phys.* **37**, R75 (2004).
- ⁹A. Laurain, M. Myara, G. Beaudoin, I. Sagnes, and A. Garnache, *Opt. Express* **18**, 14627 (2010).
- ¹⁰Z. Wang, K. Van Gasse, V. Moskalenko, S. Latkowski, E. Bente, B. Kuyken, and G. Roelkens, *Light: Science & Applications* **6**, e16260 EP (2017), original Article.
- ¹¹C. Schelte, A. Pimenov, A. G. Vladimirov, J. Javaloyes, and S. V. Gurevich, *Opt. Lett.* **44**, 4925 (2019).
- ¹²T. G. Seidel, J. Javaloyes, and S. V. Gurevich, *Opt. Lett.* **47**, 2979 (2022).
- ¹³E. R. Koch, T. G. Seidel, S. V. Gurevich, and J. Javaloyes, *Opt. Lett.* **47**, 4343 (2022).
- ¹⁴C. Schelte, P. Camelin, M. Marconi, A. Garnache, G. Huyet, G. Beaudoin, I. Sagnes, M. Giudici, J. Javaloyes, and S. V. Gurevich, *Phys. Rev. Lett.* **123**, 043902 (2019).
- ¹⁵J. Mulet and S. Balle, *Quantum Electronics, IEEE Journal of* **41**, 1148 (2005).
- ¹⁶F. Gires and P. Tournois, *C. R. Acad. Sci. Paris* **258**, 6112 (1964).
- ¹⁷B. Golubovic, R. R. Austin, M. K. Steiner-Shepard, M. K. Reed, S. A. Diddams, D. J. Jones, and A. G. V. Engen, *Opt. Lett.* **25**, 275 (2000).
- ¹⁸S. Balle, *Phys. Rev. A* **57**, 1304 (1998).
- ¹⁹K. Engelborghs, T. Luzyanina, and D. Roose, *ACM Trans. Math. Softw.* **28**, 1 (2002).
- ²⁰D. Hessel, S. V. Gurevich, and J. Javaloyes, *Opt. Lett.* **46**, 2557 (2021).
- ²¹T. G. Seidel, S. V. Gurevich, and J. Javaloyes, *Phys. Rev. Lett.* **128**, 083901 (2022).
- ²²D. A. W. Barton, B. Krauskopf, and R. E. Wilson, *Journal of Difference Equations and Applications* **12**, 1087 (2006), <https://doi.org/10.1080/10236190601045663>.
- ²³J. Knobloch and T. Wagenknecht, *Physica D: Nonlinear Phenomena* **206**, 82 (2005).
- ²⁴P. Parra-Rivas, E. Knobloch, D. Gomila, and L. Gelens, *Phys. Rev. A* **93**, 063839 (2016).
- ²⁵C. Schelte, D. Hessel, J. Javaloyes, and S. V. Gurevich, *Phys. Rev. Applied* **13**, 054050 (2020).
- ²⁶L. A. Lugiato and R. Lefever, *Phys. Rev. Lett.* **58**, 2209 (1987).
- ²⁷P. Parra-Rivas, D. Gomila, F. Leo, S. Coen, and L. Gelens, *Opt. Lett.* **39**, 2971 (2014).
- ²⁸P. Parra-Rivas, D. Gomila, and L. Gelens, *Phys. Rev. A* **95**, 053863 (2017).
- ²⁹S. V. Gurevich and J. Javaloyes, *Phys. Rev. A* **96**, 023821 (2017).
- ³⁰J. Hausen, K. Lüdige, S. V. Gurevich, and J. Javaloyes, *Opt. Lett.* **45**, 6210 (2020).
- ³¹M. Peil, M. Jacquot, Y. K. Chembo, L. Larger, and T. Erneux, *Phys. Rev. E* **79**, 026208 (2009).
- ³²J. Javaloyes, T. Ackemann, and A. Hurtado, *Phys. Rev. Lett.* **115**, 223901 (2015).
- ³³J. Mulet, M. Giudici, J. Javaloyes, and S. Balle, *Phys. Rev. A* **76**, 043801 (2007).
- ³⁴A. Gavrielides, T. Erneux, D. W. Sukow, G. Burner, T. McLachlan, J. Miller, and J. Amonette, *Opt. Lett.* **31**, 2006 (2006).
- ³⁵S.-S. Li, X.-Z. Li, J.-P. Zhuang, G. Mezosi, M. Sorel, and S.-C. Chan, *Opt. Lett.* **41**, 812 (2016).